S. Gualdi · E. Guilyardi · A. Navarra · S. Masina
P. Delecluse

The interannual variability in the tropical Indian Ocean as simulated by a CGCM

Abstract The interannual variability in the tropical Indian Ocean, and in particular the Indian Ocean dipole mode (IODM), is investigated using both observations and a multi-decadal simulations performed by the coupled atmosphere–ocean general circulation model SINTEX. Overall, the characteristics of the simulated IODM are close to the features of the observed mode. Evidence of significant correlations between sea level pressure anomalies in the southeastern Indian Ocean and sea surface temperature anomalies in the tropical Indian and Pacific Oceans have been found both in observations and a multi-decadal simulation. In particular, a positive SLP anomaly in the southeastern part of the basin seems to produce favorable conditions for the development of an IODM event. The role played by the ocean dynamics both in the developing and closing phases of the IODM events is also investigated. Our results suggest that, during the developing phase, the heat content and SST variability associated with the IODM are influenced by a local response of the ocean to the winds, and a remote response with the excitation of Kelvin and Rossby waves. Ocean wave dynamics appear to be important also during the dying phase of the IODM, when equatorial *downwelling* Kelvin waves transport positive heat content anomalies from the western to the eastern part of the basin, suppressing the zonal heat content anomaly gradient. The results obtained from the model suggest a mechanism for the IODM. This mechanism is generally consistent with the characteristics of the observed IODM. Furthermore, it might give some clue in understanding the correlation between IODM and ENSO activity found both in the model and in the observations.

S. Gualdi (✉) · A. Navarra · S. Masina
INGV, v. Gobetti 101, 40129, Bologna, Italy
E-mail: gualdi@ingv.it

E. Guilyardi
CGAM, Reading, UK

P. Delecluse
LODYC, Paris, France

1 Introduction

The climate of the tropical Indo-Pacific region exhibits a marked interannual variability, which has an enormous impact on food production and water resources in most of the tropical and subtropical countries. Therefore, the understanding of the mechanisms that produce this variability is of great importance, as well as the ability to simulate and, possibly, to forecast it with climate coupled atmosphere–ocean models.

The El Niño/Southern Oscillation (ENSO) is well recognized as the dominant mode of variability in the tropical Pacific at interannual time-scales. In the last two decades, ENSO and the variability related to it have been extensively investigated both in observations and model simulations (for a comprehensive review see Philander 1990, and the *J Geophys Res special issue on the TOGA decade*, vol 103, 1998).

The interannual variability in the tropical Indian Ocean (TIO), on the other hand, has received less attention. Until recently, most of the studies were mainly focused on the response of the Indian Ocean (IO) to the ENSO variability (e.g., Latif and Barnett 1995; Tourre and White 1997; Venzke et al. 2000). As these studies have shown, the ENSO events are followed by large-scale Sea surface temperature (SST) anomalies of the same sign in the tropical and subtropical IO, with a time lag of a few months. Venzke et al. (2000) have shown that these IO SST anomalies may be induced by net surface heat flux anomalies, which, in turn, are due to the changes in the atmospheric circulation forced by the equatorial Pacific SST anomalies.

The basin-wide SST variations, however, are not the only interannual anomalies that characterize the TIO climate variability. Reverdin et al. (1986) showed that interannual fluctuations of the zonal SST distribution

were occurring in the equatorial IO accompanied by strong surface wind and convective anomalies. Similar anomalous conditions of the TIO have also been observed during 1994 and 1997 (Behera et al. 1999; Webster et al. 1999; Saji et al. 1999). In particular, Saji et al. (1999, hereafter referred to as S99) have identified a mode of variability of the SST characterized by a zonal bipolar structure, that they called Indian Ocean dipole mode (IODM), and which explains a substantial part of the total SST variance in the TIO. The extremes of this dipole are located over the eastern and western TIO. In its positive phase, the dipole is characterized by warm SST anomalies in the western Indian Ocean and cold anomalies in the eastern Indian Ocean. The mode exhibits a pronounced seasonality in its occurrence, with the largest anomalies observed during northern autumn.

The SST anomalies are associated with convective, surface winds and sea-surface height anomalies. The air–sea feedbacks are crucial for the developing of an IODM event (Iizuka et al. 2000), indicating that this variability is the product of a coupled ocean–atmosphere mode (Webster et al. 1999; S99).

The strength of the 1994 and, particularly, 1997 IODM events has raised a notable interest in the phenomenon. Recently a number of observational and model studies have been published, showing that the IODM is an important component of the Indo-Pacific climate system (e.g., Vinayachandran et al. 2002 and references therein). Furthermore, the assessment of its influences on precipitation over eastern Africa and the Indonesian region (e.g. Black et al. 2002) has shown that the effects of the IODM might have a strong social impact over the entire region.

However, a number of important questions still need to be addressed. For example, the dynamics of the IODM, i.e., what are the mechanisms that cause the development and the decay of the observed anomalies, are still unclear. In particular, the role played by ocean dynamics in the developing and decaying phases of an IODM event is still a controversial issue (e.g., Murtugudde et al. 2000; Baquero-Bernal et al. 2002; Vinayachandran et al. 2002; Rao et al. 2002). Also, the possible relationship between IODM and ENSO is a matter of debate. Both Webster et al. (1999) and S99, in their observational studies, and Iizuka et al. (2000), in a model study, conclude that the IODM variability is independent of ENSO. However, recent works (e.g., Chambers et al. 1999; Huang and Kinter 2002, Allan et al. 2001, and references therein) suggest that the IODM and the ENSO variability do not operate in a completely independent way.

Unfortunately, the observational data sets currently available limit investigation of these controversial points. Some useful insight, however, can be gained by using general circulation model experiments.

Although a variety of fully coupled ocean–atmosphere models (CGCMs) have been developed recently, the documentation of the capability of the CGCMs to simulate the IODM variability is still very poor (Iizuka

et al. 2000). The first objective of this work is to evaluate and to document the ability of the SINTEX CGCM (Gualdi et al. 2002) to reproduce the IODM variability. The SINTEX climatology is reasonably close to the observations (Gualdi et al. 2002), and the model appears to reproduce a realistic ENSO variability (Guilyardi et al. 2002). Furthermore, with this study, we want to investigate the dynamics of the IODM, analyzing the possible role played by the ocean-wave dynamics in its evolution, and assessing the possible relationship between the IODM and interannual variability in the equatorial Pacific. The word "mode" is usually reserved to indicate a coherent pattern dynamically determined, as for instance in "normal mode". It is not clear if the IODM is such a natural mode of the TIO basin, but we will use the name for clarity of expression.

The work is organized as follows: in Sect. 2, the data and the model employed in the study are described. In Sect. 3, the capability of the model to simulate the main features of the observed climatological seasonal means and variance patterns in the TIO are assessed. The simulated IODM, its comparison with observations, and the role of the ocean dynamics are discussed in Sect. 4. In Sect. 5, we discuss a possible mechanism for the model IODM and the relation with ENSO and Sect. 6 concludes the study.

2 The data and the model used in the study

The modeling data employed in this work are time series obtained from a long (200 years) integration carried out with a coupled GCM. The results shown are obtained from an analysis performed on the entire 200 year time series. The model is SINTEX, namely the ECHAM–ORCA coupled GCM developed within the Scale INTeraction EXperiment (SINTEX) EU project.

ORCA is the global version of the OPA 8.1 ocean modeling system developed by the LODYC team in Paris (Madec et al. 1998, see full documentation at http://www.lodyc.jussieu.fr/opa/). It is a finite differences OGCM and solves the primitive equations with a non-linear equation of state on an Arakawa C-grid.

The present configuration uses a rigid lid. The horizontal mesh is orthogonal and curvilinear on the sphere. To overcome the singularity at the North Pole, the northern point of convergence has been replaced by two poles located in Asia and North America. Its space resolution is roughly equivalent to a geographical mesh of 2 by 1.5° (with a meridional resolution of 0.5° near the Equator). A total of vertical levels are used with 10 levels in the top 100 m.

Vertical eddy diffusivity and viscosity coefficients are computed from a 1.5 turbulent closure scheme which allows an explicit formulation of the mixed layer as well as minimum diffusion in the thermocline (Blanke and Delecluse 1993). Horizontal mixing of momentum is of Laplacian type with an eddy viscosity coefficient of 40,000 m^2/s, reduced in the tropics to reach 2000 m^2/s at the Equator. The lateral mixing of tracers (temperature and salinity) is "quasi-pure" isopycnal as described by Guilyardi et al. (2001). There is no interactive sea-ice model in the configuration used for the present study: sea-ice cover is relaxed towards the observed monthly climatology.

ECHAM-4 is the fourth generation of the ECHAM atmospheric general circulation model (AGCM) developed at the Max Planck Institut Für Meteorologie in Hamburg. ECHAM is an evolution of the spectral numerical weather prediction model developed at the European Center for Medium-Range Weather Forecasting (ECMWF), but significantly modified to make it suitable for climate studies.

An exhaustive and detailed description of the dynamical and physical structure, and the simulated climatology of ECHAM-4 has been given by Roeckner et al. (1996). Here we summarize briefly the main characteristics of the model. ECHAM-4 uses a semi-Lagrangian transport method for the advection of cloud water and water vapor (Rasch and Williamson 1990). The parametrization of convection is based on the mass flux concept (Tiedtke 1989), where the organized entrainment and detrainment are related to buoyancy and an adjusted-type closure based on the convective available potential energy is used (Nordeng 1994). The radiation code is the same as Morcrette (1991) with a few modifications such as the inclusion of additional greenhouse gases, revised parametrization for the water vapor continuum and for the cloud optical properties.

The model equations are solved on 19 hybrid vertical levels (top at 10 hPa) by using the spectral transform method. In this study, we used ECHAM-4 with a triangular truncation at wave number 42 (T42), which corresponds to an associated Gaussian grid of about $2.8° \times 2.8°$ in latitude and longitude.

The atmospheric and oceanic components have been coupled through OASIS 2.4 (Valcke et al. 2000). The integration was performed without any flux adjustment or restoring. Air–sea fluxes and SST were exchanged between the model components every 3 h. The coupling strategy has been described in Guilyardi et al. (2001). A complete description of the climatology simulated by the SINTEX model and an analysis of the capability of the model to reproduce the main modes of the climate variability can be found in Gualdi et al. (2002) and Guilyardi et al. (2002).

The model results are compared with those obtained from the NCEP (National Center for Environmental Predictions) re-analysis (Kalnay et al. 1996) and the HadISST1.1 Global Sea-Ice and Sea-Surface Temperature (Rayner et al. 2000) data set (hereafter HadISST). Both the observed SST and the re-analysis fields considered in this study cover the period 1958–1998.

3 The climatology of the tropical Indian Ocean

Before analyzing the details of the interannual variability, it is of some interest to discuss briefly the capability of the model to reproduce the main features of the climatology of the TIO. In particular, an important feature of this region is the pronounced seasonal signal and the marked changes in (SST), wind and precipitation patterns associated with it.

Figure 1 shows the seasonal cycle of SST and near-surface winds obtained from the HadISST and the NCEP re-analysis data sets respectively. Overall, the SST is warmer in the eastern part of the TIO, especially during the northern winter and summer. In winter (NDJFM, Fig. 1k, l, a–c), the northern part of the basin
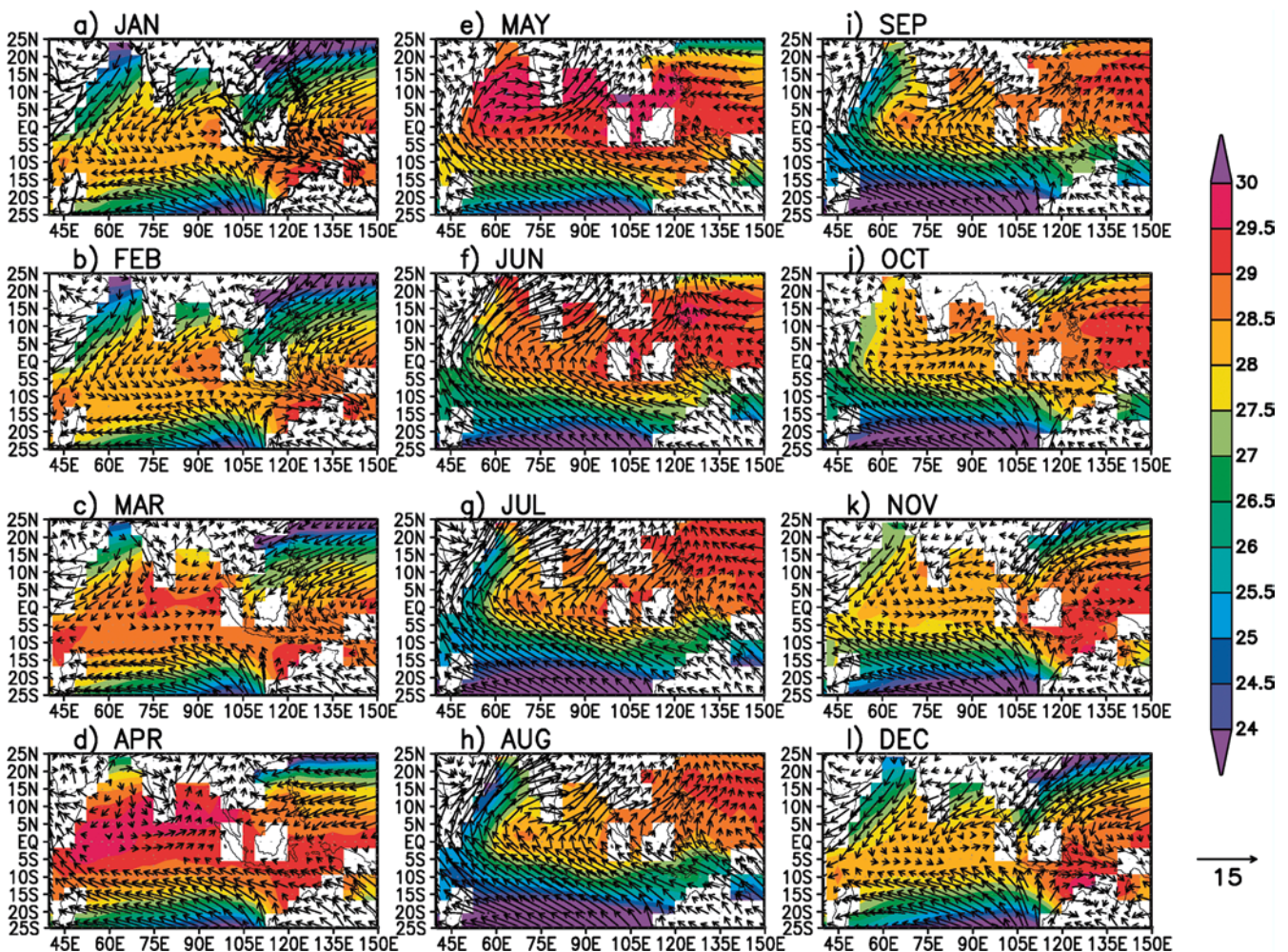

Fig. 1a–l Seasonal cycle of SST (*shaded patterns*) and 1000-hPa wind (*arrows*) in the tropical Indian Ocean, as derived from the HadISST data set and the NCEP–NCAR re-analysis respectively. The *shaded contour interval* is 0.5 °C. The reference *arrow* is 15 m/s

is characterized by northeasterly surface winds and cold SSTs. The SST has a minimum in the Arabian Sea, which extends southwestwards towards the African coast. In the southern IO, strong southeasterlies are found in the eastern part of the basin, relating to cold SSTs. In the southwest, the winds have a more pronounced (easterly) zonal component and the SST is warmer. The intertropical convergence zone (ITCZ) is centered between the equator and 10°S, where the warmest SST is located. In this region, the northeasterlies tend to turn to the east, and a narrow belt of westerlies crosses the basin.

In April (Fig. 1), warm SSTs cover most of the ocean between 10°S and 10°N. The northeasterlies are markedly reduced and westerlies extend along the equator from about 60°E to the Indonesian region.

During northern summer (MJJAS, Fig. 1e–i), the warm SST patterns have moved to the north of the equator. The surface wind flow in the northwestern IO is now reversed with respect to the northern winter. Surface southwesterlies blow from the ocean into the Indian subcontinent, carrying moisture into the regions of the Asian summer monsoon. The strong southwesterly Somali jet induces upwelling off the African and

Arabian coasts, with consequent cold SSTs, which have a minimum in August. The eastern part of the ocean has warmer SSTs. The surface winds appear to change their zonal component across the equator, being predominantly easterlies south of the equator and westerlies north of the equator.

October, like April, is a month of transition. The warm SSTs cross the equator extending to the southern part of the IO, and the surface wind along the equator is now westerly. The southwesterly jet in the western part of the basin ceases and the SSTs along the east African coast warm up.

Figure 2 shows the seasonal cycle of SST and low-level winds simulated by the SINTEX model. The overall features of the observed seasonal cycle are reproduced by the model. Although the model SST is generally slightly cooler than the HadISST case, both the SST distribution and the timing of the warm SST shift across the equator are reasonably well captured.

The winter and summer phases of the simulated Somali jet are similar to the re-analysis. However, during northern summer, the model surface southwest-
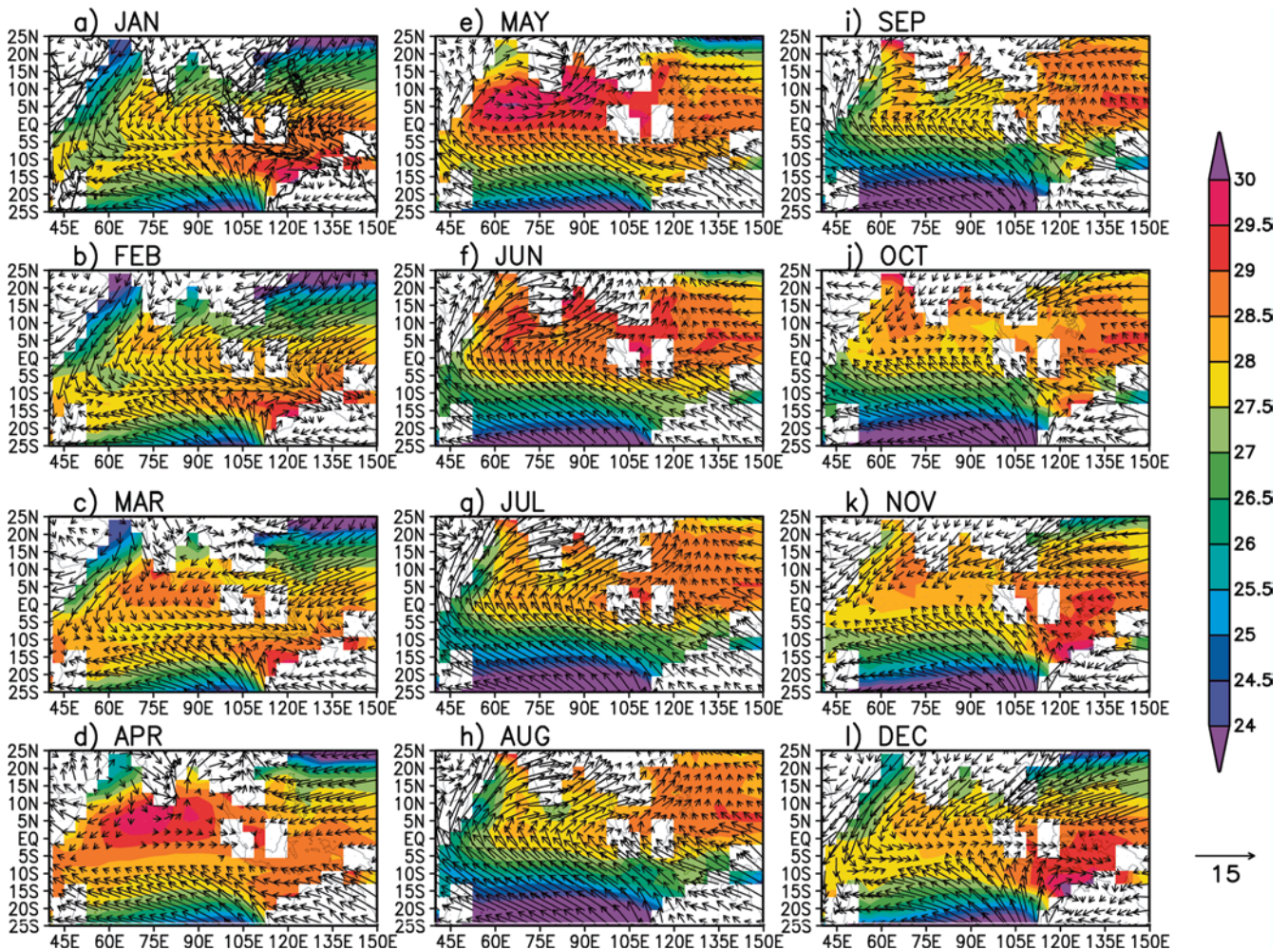

Fig. 2a–l Same as Fig. 1 but for the model

erly jet at the Somali coast appears to be slightly less intense than in the re-analysis. The reduced wind is likely the cause of a weak model upwelling in this region. Consistently, the simulated SSTs off the east African and Arabian coasts between June and September are warmer than observed.

The simulated equatorial westerlies during the transition periods (March–April and October–November) are slightly weaker than in the re-analysis. Finally, in spring, between March and April, the model SST close to the equatorial African coast is cooler than in the observations and the simulated winds tend to blow parallel to the coast. This implies a weaker inflow of oceanic moist air into the east equatorial Africa, and a consequent weaker spring precipitation over these regions (not shown).

4 The interannual variability

The seasonal features of SST and surface winds described in Figs. 1 and 2 exhibit substantial fluctuations at interannual time scales. A first assessment of this variability can be given by computing the standard deviation of these fields. Figure 3 shows the standard deviation of the HadISST SST (Fig. 3a), zonal and

meridional component of the near-surface wind obtained from the NCEP re-analysis (Fig. 3b, c), together with the correspondent fields obtained from the SINTEX model (Fig. 3d–f).

The standard deviations shown in Fig. 3 have been computed using monthly anomalies, which, in turn, have been obtained subtracting the seasonal cycle from the fields. Therefore, these standard deviations represent, in practice, the interannual variability of the considered fields.

Overall, the SST variability in the TIO appears to be weaker than in the tropical Pacific (e.g., Vinayachandran et al. 2002; Gualdi et al. 2002). In the observations (Fig. 3a), two areas of the ocean appear to be characterized by a relatively intense SST variability: the southeastern part of the basin (off the coast of Sumatra) and the western border, close to the African coast. Both the zonal and meridional wind components (Fig. 3b, c) show a maximum of variability in the southeastern Indian Ocean. The variance of the zonal component is quite large also over the central equatorial part of the basin.

In agreement with the observations, the model SST variability (Fig. 3d) has its largest values close to the Somali and Sumatra coasts. The simulated SST variance at the eastern boundary of the basin is stronger than in
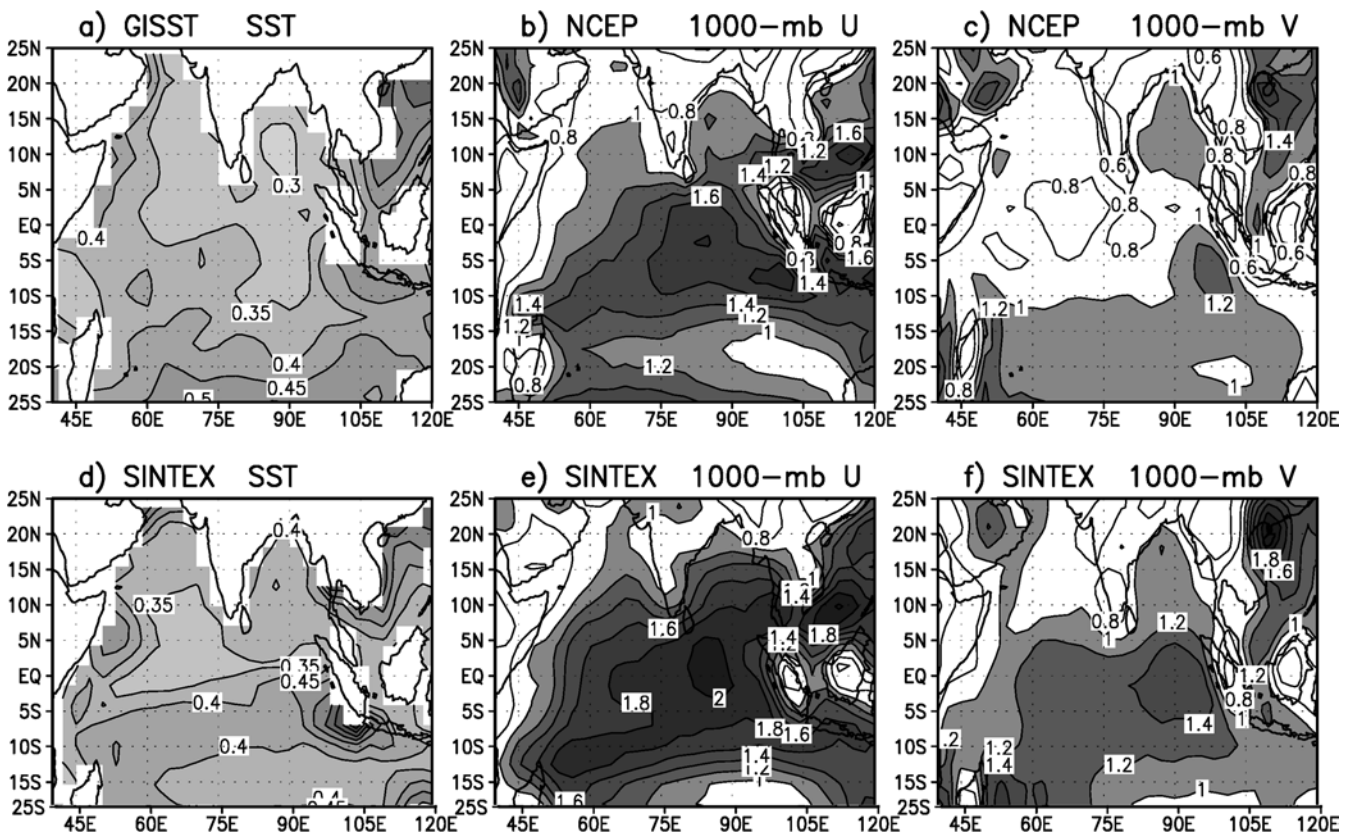
Fig. 3a–f Standard deviation of monthly anomalies; a observed SST; b, c zonal and meridional component of the 1000-hPa wind obtained from the re-analysis; d model SST; e, f zonal and meridional component of the simulated 1000-hPa wind. The contour interval for the SST standard deviation (a, d) is 0.05 °C. The contour interval for the wind standard deviation (b, c, e, f) is 0.2 m/s. Values larger than 1 m/s are *shaded*

the observations. This is consistent with the generally stronger wind variability that the model produces in the eastern part of the ocean (Fig. 3e, f). Furthermore, for both wind components, the simulated maxima of variability are shifted northward compared to the re-analysis, and are now centered on the equator. Nevertheless, the results shown in Fig. 3 indicate that the model reproduces quite well the dominant features of the variability found from the observations and re-analysis.

Some more detailed information about the characteristics of the variability depicted by the standard deviation patterns can be obtained by means of an empirical orthogonal function (EOF) analysis. S99, for instance, have applied an EOF analysis to the HadISST anomalies. Their results indicate that the variability of anomalous IO SSTs is dominated by a basin-wide mode (EOF1) related to the ENSO activity, which explains about 30% of the total SST variance. Similar results were found also by Venzke et al. (2000). The second mode of variability (EOF2) explains about 12% of the total variance, and it is characterized by a zonal bipolar structure. The extremes of this dipole are located over the western and southeastern part of the IO, in correspondence of the maximum of the SST variance shown in Fig. 3.

An EOF analysis applied to the simulated SST anomalies in the TIO produces results very close to the observational results described by S99. The variability of the modelled SST is dominated by a basin-scale mode (EOF1, not shown), which explains about 20% of the total variance. The time series of the EOF1 principal component (not shown) is well correlated ($r = 0.6$) with the NINO-3 SST anomaly time series (i.e., the most commonly used index for ENSO) with a time lag of about five months, with the NINO-3 leading.

The coupled model used in this work is able to simulate a reasonably realistic ENSO variability, as it has been described in Gualdi et al. (2002) and Guilyardi et al. (2002). However, the observed ENSO teleconnections, and in particular the influence of ENSO on the SST distribution in the tropical Indian Ocean are only partially captured by the model (Gualdi et al. 2002). This might be the reason for the relatively small variance explained by the first mode of SST variability in the tropical Indian Ocean.

The second mode (EOF2, not shown) explains about 11% of the variance and has a zonal dipole structure with characteristics very similar to the findings of S99.

In this study, we focus our analysis onto the bipolar component of the interannual variability. Following the diagnostic approach pursued by S99, the time evolution of the dipole mode is described by means of the dipole mode index (DMI), defined as the difference between the SST anomaly in the western TIO (50°E–70°E; 10°S–10°N) and the anomaly in the southeastern part of the basin (90–110°E; 10°S-Equator). As also noticed by S99, the DMI is well correlated with the principal component time series of the second EOF mode, and it can be considered representative of the fluctuations in the zonal

distribution of the SST across the TIO. The use of EOF as an indication for modes, especially bipolar modes, must be considered carefully. Orthogonality constraints may force a bipolar structure in any case. In the following, the IODM indices will be used without resorting to EOF methods.

4.1 The Indian Ocean dipole mode

The DMI time series has been computed for the entire 200 year integration. An example of the simulated DMI time series is in Fig. 4, where an 80-year chunk of the model run is shown (solid line). The results shown in this picture are fairly representative of the behavior of the simulated IODM for the rest of the integration period (200 years). Similarly to the observations, the DMI generally tends to have larger amplitudes in its positive phase. This indicates that the stronger variability is produced by anomalous conditions of the TIO characterized by cold SSTs in the southeastern part and warm SSTs in the western border. Together with the DMI, the time series of the equatorial zonal wind anomaly (averaged over the region: 70–90°E; 5°S–5°N) is also plotted (dashed curve). These results show that variations of the SST zonal distribution in the model are strongly correlated with the fluctuations of the equatorial zonal wind, as in the observations (S99).

An important feature of the observed dipole mode is its pronounced seasonality, with the anomalies that clearly peak during the northern autumn (S99). Figure 5 shows the seasonality of the DMI in its positive phase (DMI > 0), as obtained from the HadISST data set (solid line curve) and from the model (dashed curve).
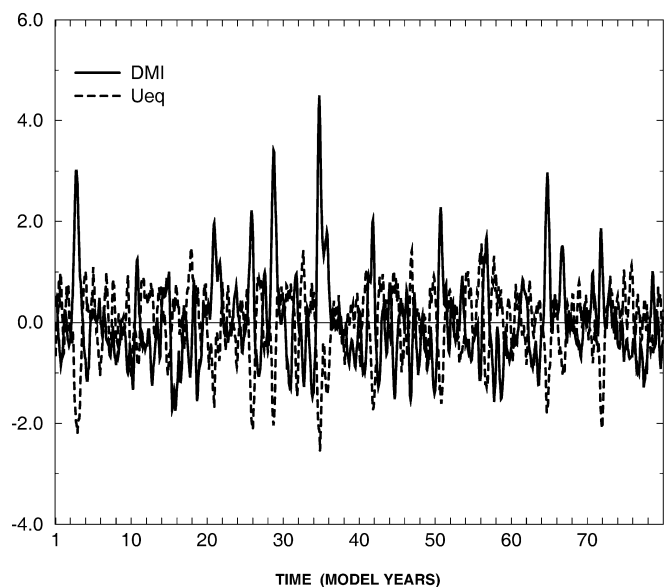
Fig. 4 *Solid line*: dipole mode index (DMI); *dashed line*: equatorial central Indian Ocean zonal wind. Both the indices have been defined as in Saji et al. (1999). The correlation between the two time series is –0.7
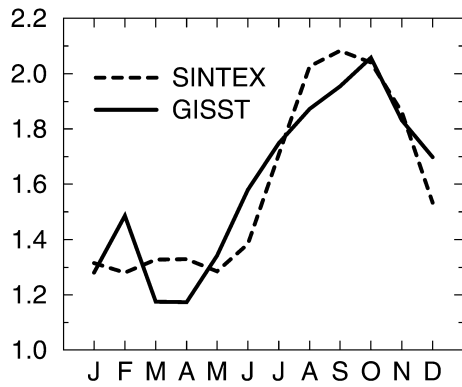
Fig. 5 Seasonality of the DMI as simulated by the model (*dashed curve*) and as obtained from the HadISST data set (*solid curve*)

The agreement between the simulated and the observed seasonal occurrence of the IODM events is quite good, though in the model the peak of the events tends to occur slightly earlier.

Additional insight into the characteristics of the dipole mode variability can be obtained by calculating composite analyses to yield the patterns of sea-level pressure (SLP) and near-surface wind anomalies that are associated with the changes in the SST field. Figure 6 shows the composite patterns obtained for the positive phase of the observed IODM. The composites are computed by averaging the anomalies corresponding to the observed events for which the DMI value is larger than 1.5 standard deviation. For the period 1958–1999, six events have been identified with such a characteristic. Specifically, they are the events during years 1961, 1967, 1972, 1982, 1994 and 1997. The sequence of the composites depicts the evolution of the "mean" IODM from May before the peak of the event throughout April of the following year.

Positive SLP anomalies (Fig. 6, contour patterns) start to develop in the southeastern Indian Ocean (IO) in late spring (May–June). The SLP anomalies are accompanied by cross-equatorial southeasterly wind anomalies (arrows) in the eastern part of the basin. The
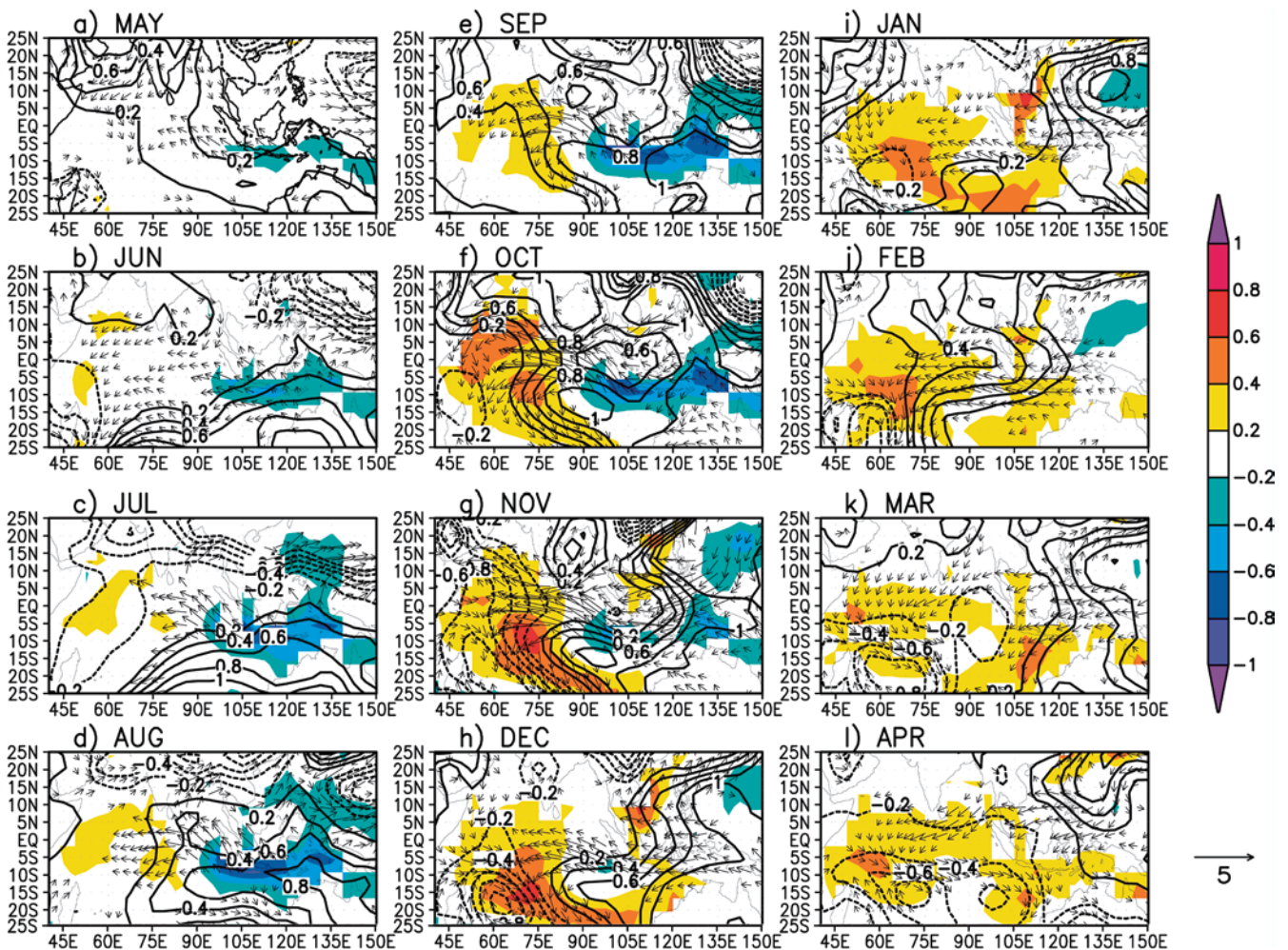
Fig. 6 a–l Composite patterns of the SST anomaly (*shaded*), 1000-hPa wind anomaly (*arrows*) and SLP anomaly (*contour*) obtained from the observations and re-analysis. The composites have been computed using the DMI as an index of the dipole mode, and by averaging the anomalies corresponding to the observed events for which the DMI value is larger than 1.5 standard deviation. For the period 1958–1999, six events have been identified with such a characteristic (1961, 1967, 1972, 1982, 1994 and 1997). *Shaded pattern* interval is 0.2 °C; *blue colors* indicate negative values, *yellow–red colors* indicate positive anomalies. Contour line interval is 0.2 hPa; negative SLP anomalies are represented with *dashed lines*. The reference arrow corresponds to a wind speed of 5 m/s

meridional component of the wind anomaly can favor upwelling along the coast of Sumatra, and, most likely due to this upwelling activity, negative SST anomalies (shaded patterns) develop in this region.

During the following summer (July–August), the anomalies intensify. Between July and August, the positive SLP anomaly in the southeastern IO moves northward towards the cold SST anomalies. Negative SLP anomalies are found over the Indian subcontinent, over Southeast Asia and in western part of the IO. The considerable north–south and east–west SLP gradient reinforces the wind anomalies, which now have also a pronounced zonal (westward) component over the equatorial central IO. Also the negative SST anomaly off Sumatra has intensified, most likely due to increased upwelling forced by the stronger wind anomaly; whereas positive anomalies start to develop in the western part of the basin.

The anomalies reach their largest values during the northern autumn, peaking between October and November. During this period the SLP anomaly exhibits two maxima, centered approximately at 10–15°N and 10–15°S, flanking the equator at about 90°E. The SLP

and wind anomaly patterns over the TIO now have the structure of the Rossby component of the atmospheric response to a negative heat anomaly centered over the equatorial eastern IO (Gill 1980). A suppressed diabatic heating in the equatorial eastern part of the basin is consistent with the observed reduced precipitation over this area during an IODM event (S99). At the same time, surface convergence is found over the warm SST anomaly in the western part of the IO, and surface equatorial westerly winds are visible at about 50°E.

During the following winter the anomalies tend to vanish. However, it is worth noticing that a large-scale positive SST anomaly persists over the entire basin until the following spring (Fig. 6i–l).

The same analysis performed on the model output produces the results shown in Fig. 7. In this case the composite patterns have been obtained by averaging 20 simulated IODM events. Furthermore, the anomalies shown in Fig. 7 satisfy a 95% significance test, which, in turn, has been assessed by means of a Monte Carlo test.

In agreement with the re-analysis, positive SLP anomalies (Fig. 7, contour patterns) start to develop in the SEIO in late spring (May–June), together with cross-
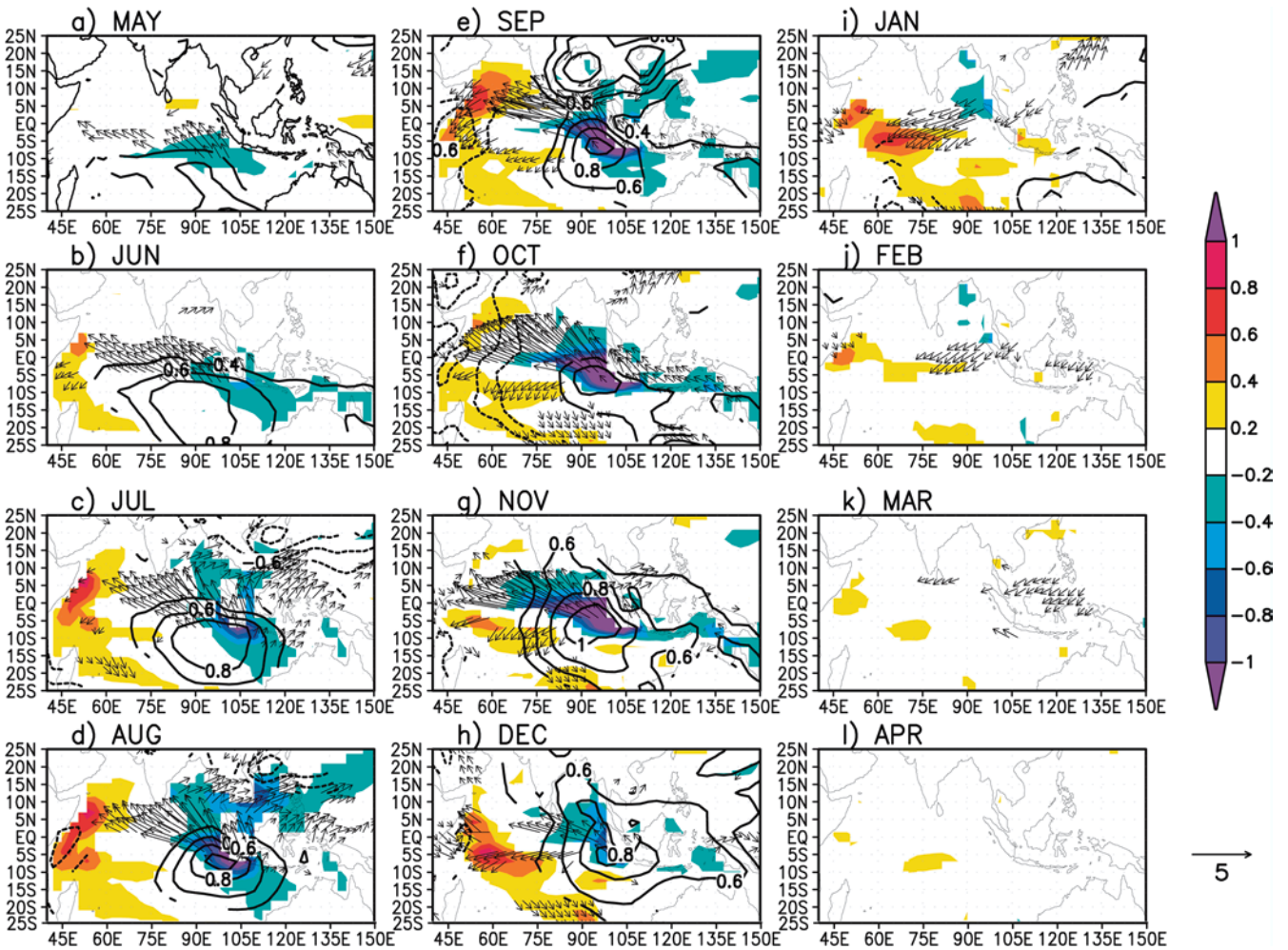
Fig. 7 a–l Same as Fig. 6 but for the model. In this case the composite patterns have been obtained by averaging 20 simulated IODM events. The plotted anomalies exceed a 95% significance level, which has been assessed with a Monte Carlo test

equatorial southeasterly wind anomalies (arrows). Overall, the simulated wind anomalies are more intense than in the re-analysis.

In a similar way to the observations, the wind anomaly exhibits a strong meridional component close to the Sumatra coast. Cold SST anomalies (shaded patterns) are found in this region, probably produced by the surface wind anomalies via equatorial and coastal upwelling. The anomalies, then grow rapidly during the following summer (July–August), and, in agreement with the re-analysis, the positive SLP anomaly moves towards the cold SSTs. The large negative SLP anomaly found in the re-analysis over Southeast Asia during this season is substantially weaker in the simulation.

At the same time, warm SST anomalies develop in the western part of the basin. At this stage of the event, the model positive SST anomalies in the western IO are larger than in the reference case. This is probably a consequence of the surface warm water piling produced by the intense surface easterly wind anomaly. Furthermore, the anomalous northeasterly wind marked at the Somali coast in July (Fig. 7c), together with the intense westward wind anomaly along the equator might also contribute to reducing the coastal upwelling in this region. This model tendency to produce a larger warm SST anomaly in the western IO during July and August, is most likely the cause for the slight advance of the simulated DMI peak occurrence with respect to the observations (Fig. 5).

As for the observations, the simulated anomalies tend to peak during northern autumn. Two SLP anomaly maxima develop over the Bay of Bengal and over the southeastern IO (Fig. 7e), and, though a little in advance with respect to the reference case, the model tends to reproduce the atmospheric Rossby response to the suppressed convection (not shown) in the equatorial eastern IO. At the same time, negative SLP anomalies have developed over the western part of the ocean.

During December (Fig. 7h), the simulated anomalies decrease in the eastern part of the basin, whereas positive SST anomalies persist in the west. In particular, a relatively intense anomaly of SST, centered at about 5°S–60°E, is associated with surface convergence and increased precipitation (not shown) over this area, and a surface eastward wind anomaly start to develop at the western boundary of the ocean.

The anomalies associated with the simulated IODM events, then, vanish quickly during the following winter and spring (Fig. 7i–l). In these months, some evidence of a persistent positive SST anomaly is visible, but it is less extended than in the observations (Fig. 6).

The composites shown in Fig. 6, for the observations, and Fig. 7, for model, have been computed by considering all the IODM events for which the DMI was larger than 1.5 standard deviations. No stratification of the events based on the ENSO phase has been performed. Therefore, these composites include the influence of ENSO on the IODM variability.

In the case of the observations, the 6 IODM events considered for the computation of the composites in Fig. 6 include three events occurring during intense warm ENSO conditions (1972, 1982 and 1997). In the model, among the 20 IODM events considered for the computation of the composites in Fig. 7, seven episodes occur during intense warm ENSO conditions. Intense warm ENSO conditions have been defined as the periods during which the NINO-3 SST anomaly index exceeds the threshold of 1.5 standard deviations for at least three consecutive months.

When the composites are computed excluding the IODM events occurring in intense ENSO conditions (not shown), both for the observations and the model, the persistent positive SST anomalies found after the termination of an IODM event (Fig. 6 and Fig. 7i–l) tend to disappear. In this case, the amplitude of the SST anomalies in the TIO after the peak of the event is small and they tend to have a rather noisy spatial structure.

On the other hand, when only the IODM events occurring during intense warm ENSO are considered, both for the observations and the model, the composites (not shown) exhibit basin-wide, large positive SST anomalies that cover most of the tropical Indian Ocean and persist throughout the northern winter and spring following the peak of the event.

These results suggest that the persistent large-scale positive SST anomalies, that characterize the tropical Indian Ocean after the termination of an IODM event as shown in Figs. 6 and 7, are most likely due to the influence of ENSO on the IODM variability.

4.2 The role of the ocean dynamics

The results shown in Figs. 6 and 7, in agreement with previous studies (e.g., Webster et al. 1999; Iizuka et al. 2000), suggest that the IODM is a coupled ocean–atmosphere phenomenon, where positive air-sea feedbacks produce the growth of the SLP, surface flow and SST perturbations. Thus, it is of interest to understand what role the ocean dynamics plays in this phenomenon. In particular, the importance of ocean wave-dynamics in the raising and decaying phases of an IODM is an important and still controversial issue (e.g., Webster et al. 1999; Murtugudde et al. 2000; Vinayachandran et al. 2002; Baquero-Bernal et al. 2002; Rao et al. 2002). Unfortunately, the limitation of the observational oceanic data sets does not allow us to draw any firm conclusion. However, some useful insights can be gained from the results obtained with the CGCM.

Thus, we have computed the composites of the upper 300-m heat content (HC) anomaly obtained from the model (Fig. 8). In late spring (May–June), consistently with the upwelling favorable wind anomalies shown in Fig. 7, negative HC anomalies develop along the equator and in the eastern part of the IO, close to the coast of Sumatra. At the same time, positive anomalies develop in the central–western part of the ocean, with two
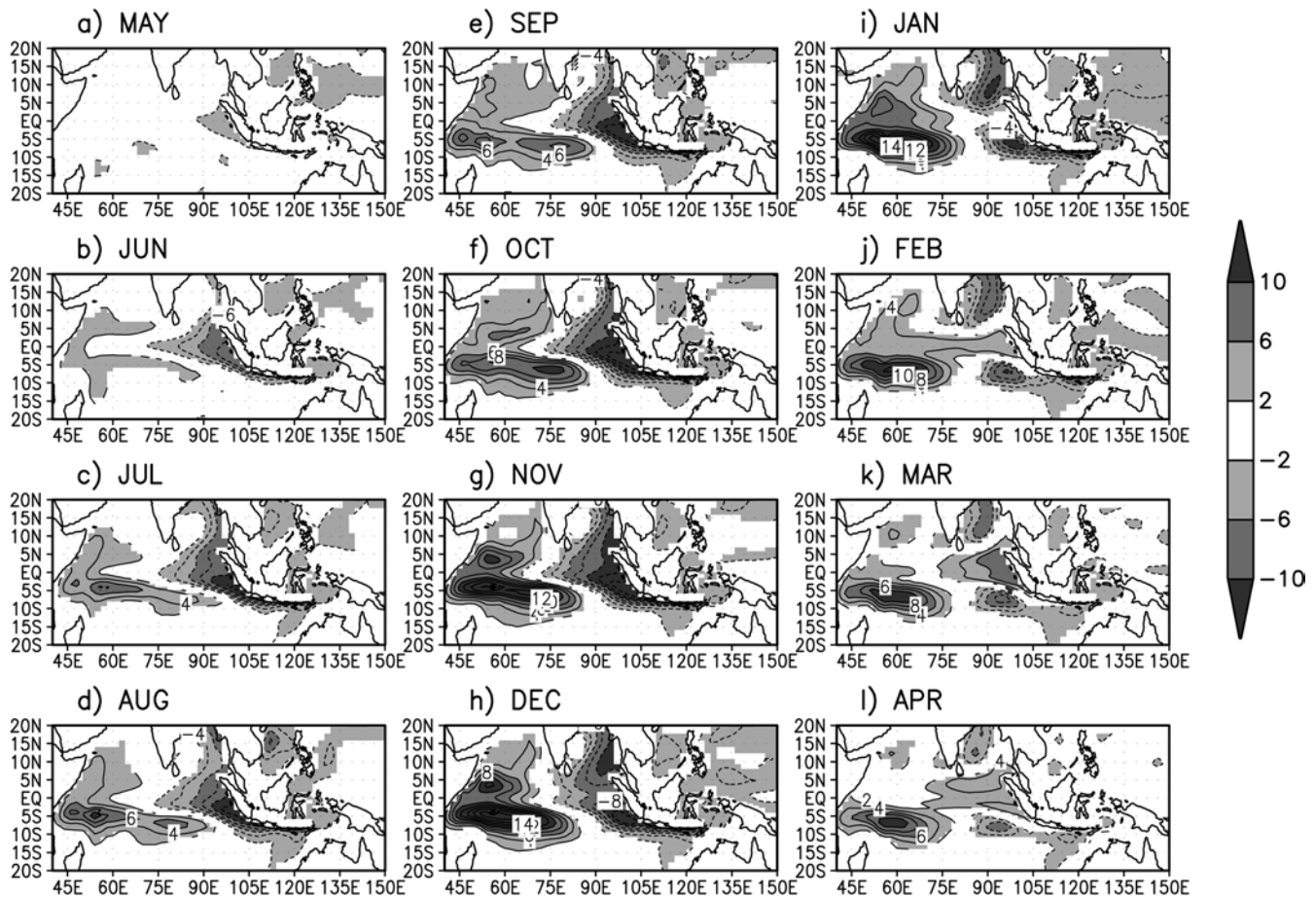
Fig. 8 a–l Composite patterns of the simulated heat content (HC). The plotted anomalies satisfy a 95% significance level, which has been assessed with a Monte Carlo test. The contour line interval is $2 \cdot 10^{+8}$ J/m^2. Shaded pattern interval is $4 \cdot 10^{+8}$ J/m^2

maxima flanking the equator at about 5°N and 5°S respectively.

During the following summer the anomalies amplify. The positive HC anomaly located south of the equator is larger than the anomaly found to the north. This might be explained by the fact that the thermocline is substantially shallower south of the equator. Therefore, small perturbations of the thermocline depth in this region might result in a large HC anomaly.

The formation and the growth of the off-equatorial HC anomalies in the central–western IO are very rapid (Fig. 8a–d), suggesting that these anomalies might be the result of a local response of the ocean to the wind anomaly. For example, they might be produced by the Ekman pumping forced by the anticyclonic surface wind anomaly south of the equator (Fig. 7).

A secondary maximum of HC anomaly is found in the central IO slightly south of the equator at about 7°S and 80°E (Fig. 8d). The anomaly maximum, then moves slowly westward as a Rossby wave, reaching the western part of the basin after a few months (Fig. 8d–h). The propagation of the HC anomaly maximum is clearly visible in a time-longitude diagram of the HC anomaly averaged between 7°S and 10°S (not shown). In agreement with the observational results of Xie et al. (2002)

and Rao et al. (2002), the maximum moves westward with a phase speed of approximately 0.15 m/s.

The anomalies peak between November and December, forming a large-scale zonal bipolar structure. Positive HC anomalies cover the TIO west of about 80°E, whereas the eastern part is almost entirely covered by negative anomalies. The anomaly extremes are located slightly south of the equator. In agreement with the findings of Rao et al. (2002), in the eastern part of the basin, the oceanic response propagates poleward as upwelling coastal Kelvin waves, affecting the ocean circulation in the Bay of Bengal.

At the same time, the signature of equatorial downwelling Kelvin waves becomes visible in the central IO (Fig. 8h, i). These equatorial Kelvin waves transport positive HC anomalies to the eastern border of the basin (Fig. 8i–l), destroying the negative anomalies accumulated there during the developing phase of the IODM and suppressing the zonal HC anomaly gradient along the equatorial IO. Finally, during the late winter and spring following the peak of the event, most of the TIO is characterized by positive HC anomalies.

As a reference, Fig. 9 shows the HC composites obtained from an ocean analysis (Masina et al. 2001). In this case, the composites have been computed by
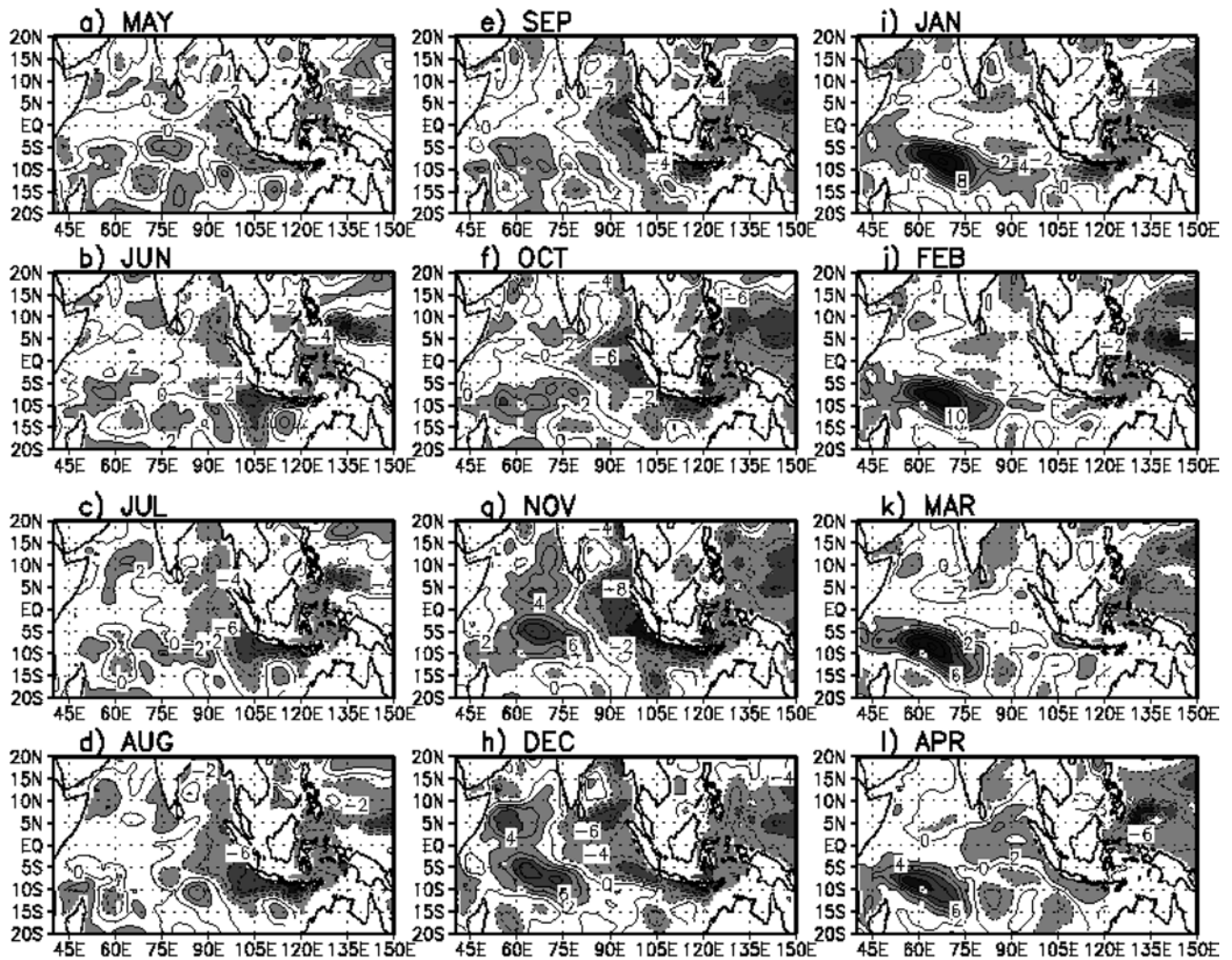
Fig. 9 a–l Composite patterns of the heat content anomaly obtained from an ocean analysis. The patterns have been computed by averaging the anomalies from two IODM events, 1982 and 1994. The contour interval is $2 \cdot 10^{+8}$ J/m^2. Shaded pattern interval is $4 \cdot 10^{+8}$ J/m^2

considering the 1982 and 1994 IODM events, therefore their statistical significance can not be fully assessed. However, it is worth noticing that the evolution of the HC anomalies obtained from the model is in general agreement with the results obtained from the oceanic analysis. A negative HC anomaly develops in the eastern part of the TIO, close to Sumatra, during late spring and summer (Fig. 9a, b). Although, the off-equatorial positive anomalies in the central–western part of the basin are weaker than in the model, they grow rapidly during the following autumn, and the HC anomaly patterns during the peak of the event (Fig. 9f–h) are very similar to the patterns obtained from the simulation. The results shown in Fig. 9 seem to confirm the model suggestion that the off-equatorial HC anomalies in the central–western IO are mainly produced locally, most likely as the result of a local response to the wind forcing. Finally, as in the model, the event appears to be terminated by the occurrence of equatorial downwelling

Kelvin waves, whose signature is visible in the equatorial IO between December and March (Fig. 9h–k).

The results shown in Fig. 8 are also consistent with the findings of Murtugudde et al. (2000) and Rao et al. (2002), suggesting that the SST variability associated with the IODM is influenced both through a local response of the ocean to the winds (shoaling and deepening of the thermocline), and through a remote response with the excitation of Kelvin and Rossby waves.

5 A mechanism for the model IODM

The sequence of the composites shown in Figs. 7 and 8 suggest a mechanism for the simulated IODM that can be summarized as follows: during the late spring and summer before the peak of the event, a large positive anomaly of SLP covers the southeastern TIO. Associated with this SLP anomaly, there are near-surface wind

anomalies, which, through coastal and equatorial up-welling, produce negative HC and SST anomalies in the equatorial and southeastern IO, which, in turn, further amplify the SLP anomaly. At the same time, a large positive HC anomaly is accumulated in the western part of the basin. This process appears to occur both through a local response of the ocean to the wind anomalies (Ekman pumping) and through the westward propaga-tion of HC anomalies as Rossby waves. Such Rossby waves have been described in several observational studies (e.g., Perigaud and Delecluse 1992; Le Blanc and Boulanger 2001; Xie et al. 2002).

During the developing stage (May–September), the anomalies intensify through positive air–sea feedbacks. Initially, the positive SLP anomaly extends over most of the southeastern IO. Then, it moves towards the negative SST anomaly off Sumatra and reduces its spatial exten-sion, increasing the SLP gradient across the TIO. The increased SLP gradient reinforces the wind anomalies, which, in turn, increase the HC and SST perturbations.

At the peak of the event, during the northern au-tumn, the large positive HC anomaly accumulated in the WIO is associated with a maximum of positive SST anomalies in this region. The warm SSTs induce surface convergence and, in particular, the surface westerly wind anomalies at the western border of the equatorial IO. These westerly anomalies might be responsible for the downwelling equatorial Kelvin waves, which appear to destroy the HC and SST anomaly gradient across the ocean, terminating the event in the following winter.

In the described mechanism, a crucial role is played by the SLP perturbation initially located over the southeastern IO. A large positive SLP anomaly, sitting over this region during the late spring–summer preced-ing the peak of the event, seems to create a condition favorable to the development of an IODM event. For the model, this suggestion is substantiated by Fig. 10, where the time series of the mean September–November DMI values (solid line) is plotted together with the mean June–August SLP anomaly averaged over the area 90–120°E; 20°S-Equator (dashed curve). The two time series are well correlated ($r = 0.7$), indicating that the simu-lated IODM events are generally preceded by anoma-lous positive SLP in the southeastern IO.

The results from the reference data (Fig. 11) appears to confirm the model findings. Also in this case, in fact, the relationship between SLP anomaly over the southeastern IO in spring–summer (dashed curve) and occurrence of IODM events (solid curve) seems to be rather robust, with a correlation of 0.67. These results, furthermore, are consistent with the results shown by Allan et al. (2001).

Figures 10 and 11 show that there are also years during which the relationship between the southeastern IO SLP anomaly and IODM occurrence appears to break down. In the reference case, for example, a strong positive SLP anomaly found in the southeastern IO during northern summer 1979 is not followed by an IODM event (Fig. 11). Similar cases can be found for the model (e.g., years 40, 95, 127 and 156 in Fig. 10).
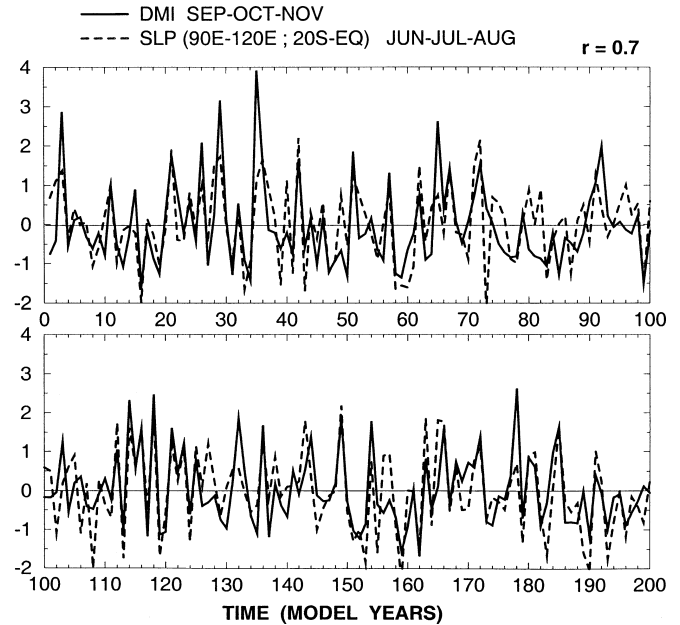
Fig. 10 *Solid line*: time series of the mean September–October–November DMI values obtained from the model; *dashed line*: mean June–July–August SLP model anomaly averaged over the area 90–120°E; 20°S-Equator. The two time series have been normalized by the respective standard deviation. The curves are well correlated ($r = 0.67$), indicating that the simulated IODM events are generally preceded by anomalous positive SLP in the southeastern IO
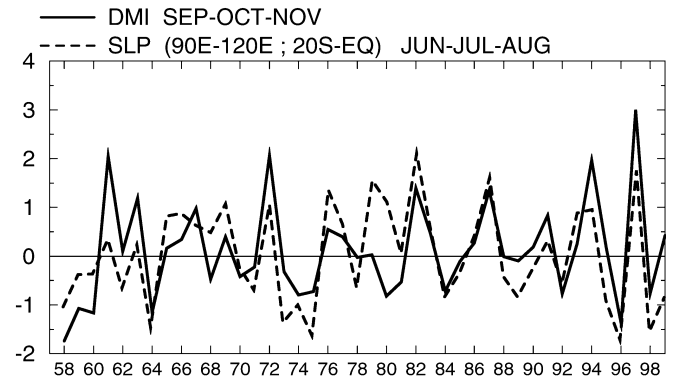
Fig. 11 Same as Fig. 10 but for the HadISST and re-analysis case. The correlation between the two curves is 0.7

There are a number of processes that might be the cause of the failed development of the IODM. Positive SLP anomaly in the southeastern IO and its associated sur-face wind anomaly create favorable conditions for the upwelling off Sumatra. However, upwelling is associated with surface cooling only if the thermocline can interact actively with the mixed layer. When this link is broken, as, for example when there is a strong barrier layer (e.g., Masson et al. 2002), then the IODM mechanism described cannot fully operate.

Another possible explanation for the failed develop-ment of IODM events even if conditions seem to be favorable, could be found in the action of intraseasonal activity. In particular the Madden–Julian Oscillation

(MJO, Madden and Julian 1994) might play an important role, as it can induce oceanic equatorial Kelvin waves (Hendon et al. 1997), which, in turn, might interfere and possibly obstruct the development of an IODM. The MJO activity has a pronounced seasonality with the strongest activity occurring in northern winter and spring (Madden and Julian 1994; Gualdi and Navarra 1998). However, in 1979 it was anomalously active also during northern summer (Lorenc 1984). Thus, the strong MJO activity observed during the northern summer of 1979, and the consequent intense oceanic intraseasonal activity might be responsible for the failed development of an IODM event in this year.

The suggestion of a possible interaction between intraseasonal activity and development of IODM events is also confirmed by the results obtained with the model. Figure 12 shows the Hovmoeller diagram of the equatorial HC anomaly from March to December of year 127 of the model simulation. This year is representative of the model cases for which there is no development of an IODM event, though the conditions appear to be favorable (i.e., intense positive SLP anomaly in the southeastern IO).

Consistently with the developing phase of an IODM event as shown in Fig. 8, Fig. 12 shows that a large negative HC anomaly starts to develop in the eastern
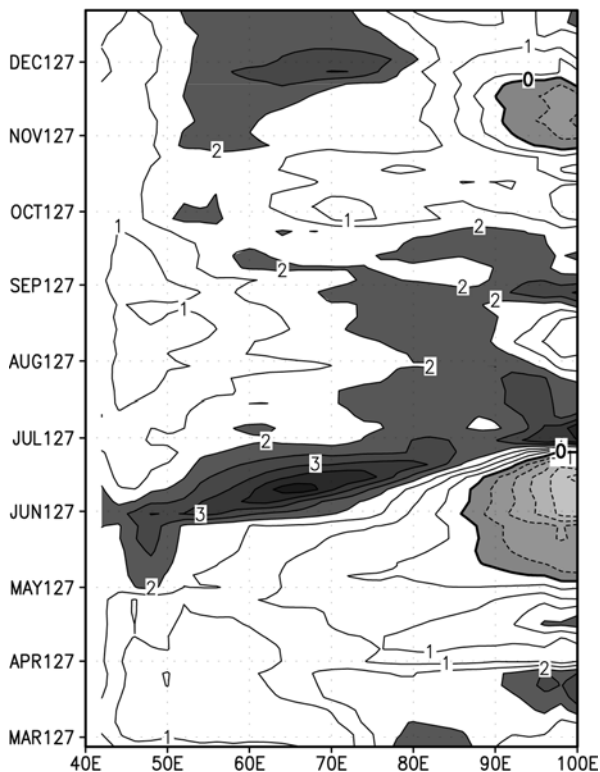
Fig. 12 Hovmoeller diagram of the equatorial HC anomaly obtained from the model for the period March year 127–December year 127. The plotted anomalies are pentads (5-day means) averaged between 2.5°S and 2.5°N. The contour interval is $0.5 \cdot 10^{+9}$ J/m². *Dark shaded* areas indicate positive anomalies larger than $2 \cdot 10^{+9}$ J/m². *Light shaded* areas indicate negative anomalies

part of the equatorial IO between May and June. The growth of the negative anomaly, however, is abruptly interrupted by the occurrence of a downwelling Kelvin wave, which is originated in the western part of the basin, and reaches the eastern boundary in July.

These results, therefore, suggest that the presence of a strong and persistent positive SLP anomaly in the SEIO and the consequent low-level wind anomalies in the TIO represent a condition favorable for the development of an IODM. However, the occurrence of an event can also be conditioned either by the subsurface precondition (e.g., Vinayachandran et al. 1999; Annamalai et al. 2002) and by the intraseasonal activity of the coupled atmosphere–ocean system.

5.1 The IODM mechanism and the ENSO variability

Whether the IODM is independent or not of the ENSO variability is a matter of active debate (e.g., Allan et al. 2001 and references therein). In their works, Webster et al. (1999) and S99 claimed that the IODM variability is independent of ENSO. Basically, they draw this conclusion by noticing that IODM events have been observed either in the absence of ENSO conditions (e.g., 1961), in La Niña years (e.g., 1967), in weak El Niño (e.g., 1994) and strong El Niño conditions (e.g., 1997). Iizuka et al. (2000) arrived at similar conclusions analyzing the IODM simulated with a CGCM.

Actually, if the DMI and the NINO-3 SST anomaly time series (NINO-3 SSTA) are compared, their correlation is poor (S99). However, as shown for instance by Baquero-Bernal et al. (2002) and Allan et al. (2001), the correlation between the two time series increases substantially and becomes significant if it is computed using monthly or seasonally stratified values of the indices. For example, using the HadISST data set, Allan et al. (2001) showed that the correlation between mean September–November values of the DMI and NINO-3 SSTA is 0.52, for the period 1872–1997. The correlation, then, increases to 0.56 when computed for the period considered in S99 (1958–1997).

As it has been shown in Sect. 4, the peak of the anomalies associated with an IODM event tends to occur during northern autumn, and the maximum of the DMI occurs in this season, between October and November. If the NINO-3 SSTA is used as an index for ENSO, the ENSO peak tends to occur between December and February. Thus, the maximum of the DMI tends to occur slightly in advance of the NINO-3 SSTA peak.

Using the HadISST data set, we have computed the correlation between the DMI and the NINO-3 SSTA seasonal time series. The results indicate that the correlation is maximized when autumn values (September–November) are considered for the DMI, and winter values (December–February) are considered for the NINO-3. In this case the value of the correlation is larger than 0.6.

The IODM mechanism described in the previous section might give some insight into how a possible

Fig. 13 Time series of the
simulated NINO-3 SSTA (*solid
line*) and SLP anomaly
averaged as in Fig. 10 (*dashed
curve*). The curves show
monthly mean values, and have
been normalized by the
respective standard deviation.
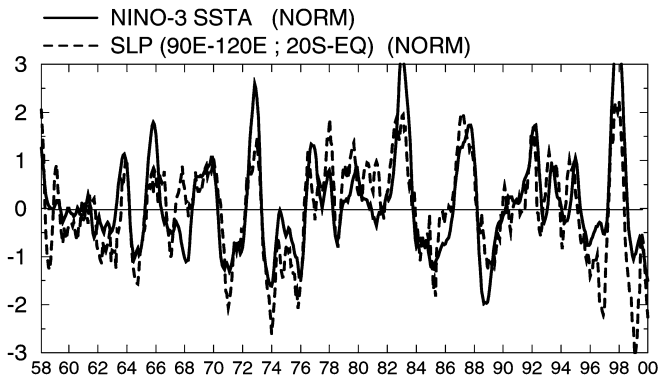The correlation between these
two curves is 0.7
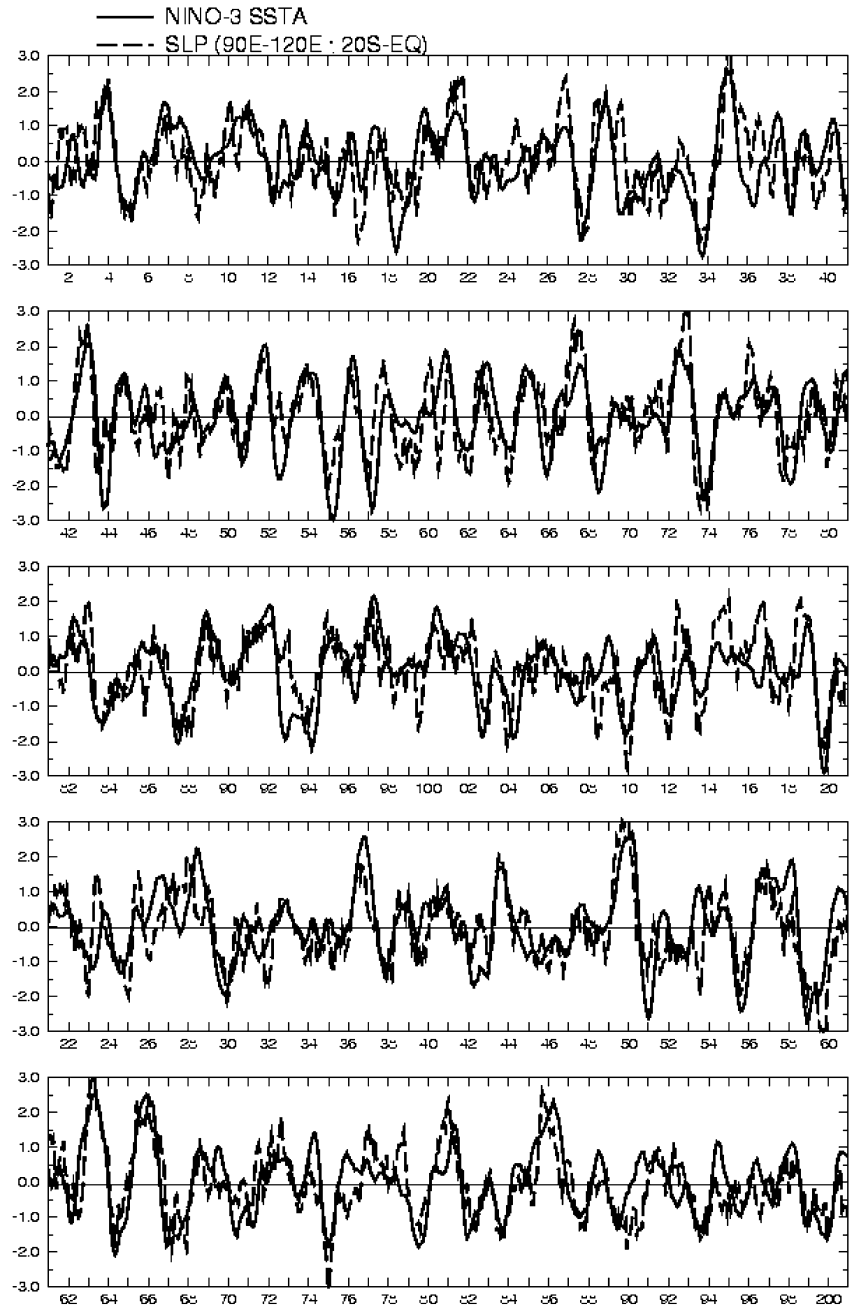
ENSO–IODM link might occur. In Figs. 13 and 14, the
monthly mean time series of NINO-3 SSTA are plotted
together with the monthly mean SEIO SLP anomaly for
the model and the reference case respectively. As these
show, the interannual variability of the southeastern IO
SLP is generally very well correlated with the ENSO
variability. This might be explained by the fact that the
Southern Oscillation, the atmospheric component of
ENSO, is a large-scale coherent signal, with a marked
signature in the southeastern IO (Trenberth and Shea
1987; Philander 1990). During its negative phase (El Niño
condition), the Southern Oscillation is associated with
positive SLP anomalies over the southeastern IO. Since
the presence of positive SLP anomalies over this region,

in turn, seems to be related to the possible development of
IODM events, it turns out that in its developing phase an
ENSO episode might produce conditions favorable for
the occurrence of a dipole mode in the IO.

6 Summary and conclusions

In this study, we have analyzed the interannual vari-
ability in the TIO as simulated by a coupled GCM, fo-
cusing in particular, on the dipole mode variability
recently described in several observational works. Our
main objectives were to evaluate the capability of the
model to reproduce the observed variability and identify

Fig. 14 Same as in Fig. 13, but for the HadISST and re-analysis. In this case the correlation between the two curves is 0.76

the mechanisms that might be responsible for the evolution of this mode of variability.

To this aim we have analyzed the outputs of a 200-year experiment performed with the model and compared the model results with the results obtained from observational (HadISST) and re-analysis (NCEP–NCAR) data sets.

Before analyzing the simulated interannual variability, we have assessed the ability of the model to reproduce the mean seasonal cycle in the TIO. In general, the model SST and near-surface wind seasonal means are reasonably close to the observations. The model, however, exhibits some problems in simulating the SST seasonal variation at the western border of the basin. During northern summer, in particular, the model SST at the Somali coast is too warm. This might be due to a weak Somali jet, which, in turn, might be caused by the difficulty of the atmospheric model component in reproducing the summer Asian monsoon (Roeckner et al. 1996).

The IODM variability has been identified and its evolution has been described by means of the DMI as defined by S99. In particular, the index has been used to compute composites of sea-level pressure and near-surface wind anomalies that are associated with the changes in the SST field, during an intense IODM event in its positive phase.

Overall, the evolution of the simulated anomalies is close to the results obtained from the re-analysis, and the main features of the simulated IODM are very similar to the features of the observed mode (e.g., S99). However, also notable differences are visible. In particular, the model SLP anomaly patterns exhibit some significant difference with respect to the reference case. In the re-analysis, during the developing phase of the IODM (July–August), the SLP anomalies exhibit a marked north/south contrast. Large positive anomalies are found in the southern IO, and intense negative anomalies cover the Indian subcontinent, Southeast Asia and western Pacific.

In the model, the negative SLP anomaly over India and Southeast Asia is less pronounced. This might be due to the tendency of ECHAM-4 to underestimate the convective precipitation (diabatic heating) over these

regions during the summer phase of the Asian monsoon (Roeckner et al. 1996).

The SLP anomaly distribution found from the re-analysis is consistent with the lateral monsoon circulation described by Webster et al. (1998) and Slingo and Annamalai (2000). This result seems to suggest that the Asian summer monsoon, and in particular an anomalously strong lateral monsoon circulation, might play a role in determining conditions favorable to the development of the observed IODM event. This mechanism, on the other hand, appears to be less effective in the simulated IODM. However, one should keep in mind that the composites for the reference case are obtained from a small number of IODM events (six for the re-analysis, 20 for the model). Therefore, some detail of the patterns obtained from the re-analysis might be affected by some bias and their statistical significance may be rather poor.

The results obtained from the simulated heat content are in agreement with the findings of Murtugudde et al. (2000) and Rao et al. (2002), suggesting that the SST variability associated with the IODM is influenced both through a local response of the ocean to the winds (shoaling and deepening of the thermocline), and through a remote response with the excitation of Kelvin and Rossby waves. In particular, ocean wave dynamics seems to be important during the decaying phase of the IODM, when equatorial Kelvin waves transport positive HC anomalies from the western to the eastern border of the basin, suppressing the zonal HC anomaly gradient along the equatorial IO.

Our model results suggest a possible mechanism for the IODM. This mechanism might also explain the correlation between IODM and ENSO activity found both in the model and in the observations. During the developing phase of an ENSO episode, positive SLP anomalies are created in the southeastern part of the TIO. The associated atmospheric circulation perturbations, and especially the southeasterly wind anomalies, seem to produce conditions favorable for the development of an IODM event. The ENSO remote effect, thus, appears to provide the preconditioning to set the stage for the development of the IODM, but the dynamical processes that characterize the Tropical Indian Ocean (e.g., monsoons, intraseasonal variability, etc.) are those that then determine the further evolution of the event.

Although the simulated IODM is remarkably similar to the observed mode, we have noticed that there are also important differences between the model results and the observations. These differences might mean that the described modeled mechanism may be only partially active in the real world, and that in nature other mechanisms can also be at work. However, the mechanism suggested by the simulated IODM is consistent with several characteristics of the observed IODM.

References

Allan R, and Coauthors (2001) Is there an Indian Ocean dipole, and is it independent of the El Niño–Southern Oscillation? Newsletter Climate Variability and Predictability Programme, 6(3): 18–22 Southampton, UK. Available also at http:// www.clivar.org

Annamalai H, Murtugudde R, Potemra J, Xie S-P, Wang B (2002) Coupled dynamics in the Indian Ocean: externally or internally forced? Deep-Sea Res (in press)

Baquero-Bernal A, Latif M, Legutke M (2002) On dipole-like variability of sea surface temperature in the tropical Indian Ocean. J Clim 15: 1358–1368

Black E, Slingo JM, Sperber K (2002) An observational study of the relationship between excessively strong Short Rains in coastal East Africa and Indian Ocean SST. Mon Weather Rev (in press)

Behera SK, Krishnam S, Yamagata T (1999) Anomalous air–sea coupling in the southern tropical Indian Ocean during the boreal summer of 1994. Geophys Res Lett 26: 3001–3004

Blanke B, Delecluse P (1993) Low frequency variability of the tropical Atlantic ocean simulated by a general circulation model with mixed layer physics. J Phys Oceanogr 23: 1363–1388

Chambers DP, Tapley BD, Stewart RH (1999) Anomalous warming in the Indian Ocean coincident with El Niño. J Geophys Res 104: 10,525–10,533

Gill AE (1980) Some simple solutions for heat-induced tropical circulation. Q J R Meteorol Soc 106: 447–463

Gualdi S, Navarra A (1998) A study of the seasonal variability of the tropical intraseasonal oscillation. Global Atmos Ocean Syst 6: 337–372

Gualdi S, Navarra A, Guilyardi E, Delecluse P (2002) Assessment of the tropical Indo-Pacific climate in the SINTEX CGCM. Ann Geophys (in press)

Guilyardi E, Madec G, Terray L (2001) The role of lateral ocean physics in the upper ocean thermal balance of a coupled ocean–atmosphere GCM. Clim Dyn 17: 589–599

Guilyardi E, Delecluse P, Gualdi S, Navarra A (2002) Mechanisms for ENSO phase change in a coupled GCM. J Clim (in press)

Hendon HH, Liebmann B, Glick JD (1997) Oceanic Kelvin waves and the Madden-Julian Oscillation. J Atmos Sci 55: 88–101

Huang B, Kinter III JL (2002) The interannual variability in the tropical Indian Ocean. J Geophys Res (in press)

Iizuka S, Matsuura T, Yamagata T (2000) The Indian Ocean SST dipole simulated in a coupled general circulation model. Geophys Res Lett 27: 3369–3372

Kalnay E, and Coauthors (1996) The NCEP/NCAR 40-year Reanalysis Project. Bull Am Meteorol Soc 77: 437–471

Latif M, Barnett TP (1995) Interaction in the tropical Oceans. J Clim 8: 952–964

Le Blanc J-L, Boulanger J-P (2001) Propagation and reflection of long equatorial waves in the Indian Ocean from TOPEX/ POSEIDON data during the 1993–1998 period. Clim Dyn 17: 547–557

Lorenc AC (1984) The evolution of planetary-scale 200 mb divergent flow during the FGGE year. Q J R Meteorol Soc 110: 427–441

Madec G, Delecluse P, Imbard M, Levy C (1998) OPA version 8.1 ocean general circulation model reference manual. Technical Report, LODYC/IPSL, Note 11, Paris, France, pp 91

Madden RA, Julian PR (1994) Observations of the 40–50 day tropical oscillation – a review. Mon Weather Rev 122: 814–837

Masina S, Pinardi N, Navarra A (2001) A global ocean temperature and altimeter data assimilation system for studies of climate variability. Clim Dyn 17: 687–700

Masson S, Delecluse P, Boulanger J-P, Menkes C (2002) A model study of the seasonal variability and formation mechanisms of the barrier layer in the eastern equatorial Indian Ocean. J Geophys Res 107: 8017–8037

Morcrette JJ (1991) Radiation and cloud radiative properties in the European centre for medium range weather forecasts forecasting system. J Geophys Res 96: 9121–9132

Murtugudde RG, McCreary JP, Busalacchi AJ (2000) Oceanic processes associated with anomalous events in the Indian Ocean with relevance to 1997–1998. J Geophys Res 105: 3295–3306

Nordeng TE (1994) Extended versions of the convective parameterization scheme at ECMWF and their impact on the mean and transient activity of the model in the Tropics. ECMWF Research Department, Techn Mem 206, October 1994, European Center for Medium Range Weather Forecasts, Reading, UK, pp 41

Perigaud C, Delecluse P (1992) Annual sea level variations in the southern tropical Indian Ocean from Geosat and shallow water simulations, J Geophys Res 97: 20,169–20,178

Philander SGH (1990) El Niño, La Niña and the Southern Oscillation. Academic, San Diego, California, pp 293

Rao SA, Behera SK, Masumoto Y, Yamagata T (2002) Interannual variability in the tropical Indian Ocean with special emphasis on the Indian Ocean Dipole. Deep-Sea Res 49: 1549–1572

Rasch PJ, Williamson DL (1990) Computational aspects of moisture transport in global models of the atmosphere. Q J R Meteorol Soc 116: 1071–1090

Rayner NA, Parker DE, Frich P, Horton EB, Folland CK, Alexander LV (2000) SST and sea-ice fields for ERA40. Proc 2nd WCRP International Conference on reanalyses, Reading UK August 1999, WCRP-109, WMO/TD-985: 18–21

Reverdin G, Cadet D, Gutzler D (1986) Interannual displacements of convection and surface circulation over the equatorial Indian Ocean. Q J R Meteorol Soc 112: 43–67

Roeckner E, and Coauthors (1996) The atmospheric general circulation model Echam-4: model description and simulation of present-day climate. Max-Planck-Institut für Meteorologie, Rep 218, Hamburg, Germany, pp 90

Saji NH, Goswami BN, Vinayachandran PN, Yamagata T (1999) A dipole mode in the tropical Indian Ocean. Nature 401: 360–363

Slingo JM, Annamalai H (2000) 1997: the El Niño of the century and the response of the Indian summer monsoon. Mon Weather Rev 128: 1778–1797

Trenberth KE, Shea DJ (1987) On the evolution of the Southern Oscillation. Mon Weather Rev 115: 3078–3096

Tiedtke M (1989) A comprehensive mass flux scheme for cumulus parametrization in large-scale models. Mon Weather Rev 117: 1779–1800

Tourre YM, White WB (1997) Evolution of ENSO signals over the Indo-Pacific domain. J Phys Oceanogr 27: 683–696

Valcke S, Terray L, Piacentini A (2000) The OASIS coupler user guide version 2.4. Technical Report, TR/CMGC/00-10, CERFACS, Toulouse, France, pp 85

Venzke S, Latif M, Villwock A (2000) The coupled GCM ECHO-2, part II: Indian Ocean response to ENSO. J Clim 13: 1371–1383

Vinayachandran PN, Saji NH, Yamagata T (1999) Response of the equatorial Indian Ocean to an unusual wind event during 1994. Geophys Res Lett 26: 1613–1615

Vinayachandran PN, Iizuka S, Yamagata T (2002) Indian Ocean dipole mode events in an ocean general circulation model. Deep-Sea Res (in press)

Webster PJ, Palmer TN, Yanai M, Shukla J, Magnana V, Yasunari T, Tomas R (1998) The monsoon: processes, predictability and prediction. J Geophys Res 103: 14,451–14,510

Webster PJ, Moore AM, Loschnigg JP, Leben RR (1999) Coupled ocean–atmosphere dynamics in the Indian Ocean during 1997–98. Nature 401: 356–360

Xie S-P, Annamalai H, Schott FA, McCreary Jr JP (2002) Structure and mechanisms of south Indian Ocean climate variability. J Clim 15: 864–878